Preliminary Study of an Aerial Manipulator with Elastic Suspension

Arda Yigit, Gustave Grappe, Loïc Cuvillon, Sylvain Durand, Jacques Gangloff

Preliminary Study of an Aerial Manipulator with Elastic Suspension

Arda Yiğit, Gustave Grappe, Loïc Cuvillon, Sylvain Durand, Jacques Gangloff
ICube Laboratory, Strasbourg University, UMR CNRS 7357, Strasbourg, France
Emails: gustave.grappe@gmail.com, {arda.yigit, l.cuvillon, sdurand, jacques.gangloff}@unistra.fr

***Abstract*— This paper presents a preliminary study of an Aerial Manipulator suspended by a spring to a robotic carrier. The suspended aerial manipulator is actuated by six pairs of contra-rotating propellers generating a 6-DoF wrench. Simulations show path following results using a computed torque (feedback linearization) control strategy. Active vibration canceling is validated experimentally on a first prototype.**

I. Introduction

Aerial manipulation combines the large workspace capabilities of Unmanned Aerial Vehicles (UAVs) with the dexterity and accuracy of robotic manipulators. Various configurations can be found, from simple flying hands where a gripper is attached to a UAV, to more complex flying manipulators where usually a single serial manipulator, or sometimes even multiple robotic arms, are attached to an aerial carrier [1], [2]. The aerial carrier and the robot may be tightly coupled or linked by a cable so that the robotic platform is suspended below the aerial carrier. The cable length may be controlled by a winch on the carrier side or on the robot side. Controlling additional degrees of freedom due to the swinging of the robot below the aerial carrier is a challenging problem that can be solved by active stabilization techniques involving for example actuated moving masses [3].

In [4], Zhang *et al.* suggest a bioinspired way to stabilize an aerial platform. Like a spider, the system is able to launch anchors on nearby walls and ceiling to perch and stabilize the platform. This is a low-power way of generating a constant wrench but it relies on nearby compatible anchoring surfaces.

Another approach is to use thrusters [5], [6] on the platform holding the robot as a wrench generator. The advantage of this approach is its ability to generate constant forces and moments during a long time, whereas techniques based on inertial effects like with moving masses, rotating masses, control moment gyros or reaction wheels, are prone to saturation. In [6], the authors use four ducted fans attached to a platform holding a gripper to actively compensate for the swing of this wire-suspended hand system. The swing-suppression algorithm uses Inertial Measurement Unit (IMU) measurements fed back to a PD controller. In [5], the authors introduce the concept of Suspended Aerial Manipulator (SAM). The SAM is suspended under an aerial carrier (e.g. a helicopter) by means of cables. In this work, the SAM is carrying a 7-DoF serial manipulator and is equipped with 3 actuated winches, 8 propulsion units arranged to produce an omnidirectional 6-DoF wrench, a landing gear and various sensors (IMU, GPS and two cameras). A propulsion unit is made of a brushless DC motor driving a propeller. The aerial carrier is assumed to be approximately static. The pose of the SAM is regulated using a cascade control scheme where the control input is a desired wrench acting on the SAM. This wrench is generated using the 8 propulsion units. Note that a similar concept exists in the field of underwater robotics [7]. Here the carrier consisting in an offshore platform is static, but it could be replaced by multiple moving boats holding each one cable.

In this work, we propose to suppress the SAM aerial carrier and replace it with a crane-like robotic carrier (see Fig. 1). Furthermore, in order to compensate for the gravity, reduce power consumption and simplify the mechanical design, we propose to replace the cable+winch subsystem with a low-stiffness spring with a very long elastic range. Since our team has a long background in cable-driven parallel robotics and especially in active vibration damping of such robots [8], [9], we focus here on similar robotic tasks, i.e. tasks covering a relatively large workspace (larger than with industrial manipulators but, of course, smaller than systems using an aerial carrier) with medium accuracy (sub-centimetric) and fast dynamics. These tasks include pick and place of parcels in logistic hubs, automated ship building, 3D construction printing, washing or painting of building walls. A static anchoring point may be available in all these situations: a gantry crane in a logistic hub or on a shipyard, a tower crane for 3D construction and a window-cleaning platform carrier for operations on building vertical surfaces.

The paper is organized as follows. Section II describes the design of the AMES. Section III explains the dynamic modeling. The control law is presented in Section IV. Section V introduces the dynamic simulator. Experimental results for stabilization are shown in Section VI.

II. Robot description

We designed the Aerial Manipulator with Elastic Suspension (AMES) shown in Fig. 1. An aerial manipulator is suspended at the tip of a crane-like robotic carrier by a spring. The aerial manipulator, which is called here an Aerial Wrench Generator (AWG), is holding a gripper. The AWG function is to generate a 6-DoF wrench at the end-effector of the AMES thanks to 6 propulsion units. Each propulsion unit is made of two thrusters with contra-rotating propellers. So the AMES with its robotic carrier, spring and AWG may be considered as a new kind of robot, a hybrid between a serial manipulator and an aerial manipulator with the spring acting as a flexible linkage. We called this robot "DextAir".

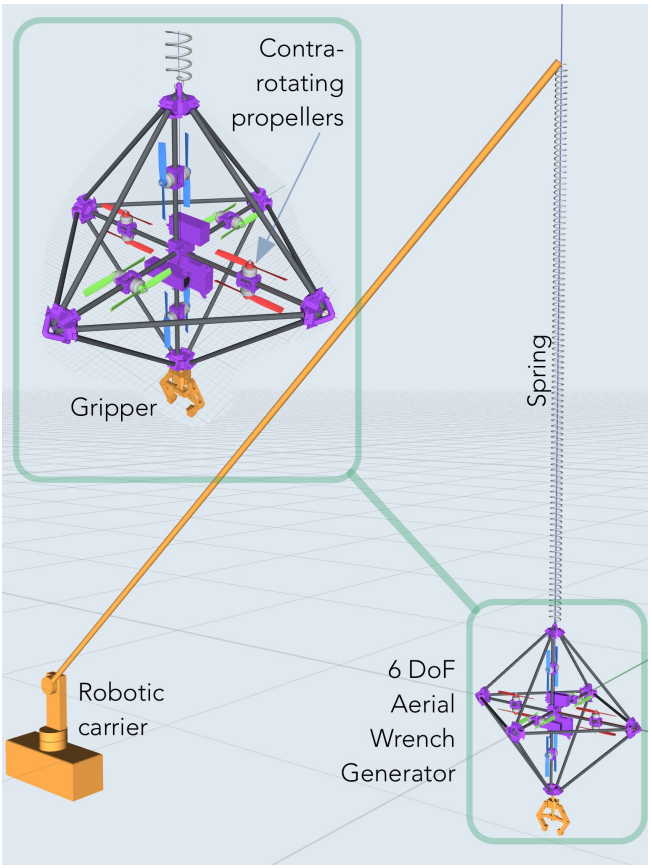

Fig. 1. DextAir concept.

The robotic carrier is optional: it is useful to extend the workspace of the robot, but with a static anchoring point of the spring, the workspace may already be large enough for many tasks. The spring has two functions: it compensates for the AWG gravity and avoids using a winch-actuated cable. The spring is also fully decoupling the vertical dynamics of the AWG from the dynamics of the carrier: it is almost free-floating in the air around its equilibrium point. Of course, in order to maximize the workspace of the gripper, the stiffness of the spring must be very low while its maximum elongation should be very high. Indeed, let k be the stiffness of the spring and F_{Zmax} be the maximum vertical force generated by the AWG. The maximal vertical displacement of the AWG starting from its equilibrium point is F_{Zmax}/k. So in order to maximize the vertical displacement, k has to be minimized. The same kind of reasoning applies to the five other degrees of freedom and yields an external boundary of the reachable workspace for a given position of the spring anchoring point. Of course, the more practical wrench feasible workspace is smaller and included within the reachable workspace [10]. The function of the robotic carrier is to move slowly the equilibrium point of the AWG to the average position of the current task. Repositioning the center of the workspace around the current task reduces the energy dissipated by the AWG's propellers when driving the high-speed displacements of the gripper. Note that since gravity is almost fully compensated by the spring, the AWG, unlike a drone, requires very little energy.

The AWG has the same structure as an omnidirectional multirotor vehicle described in [11] where the relative placement of propulsion units is optimized to maximize the agility. We selected the optimal configuration for $N = 6$ propulsion units (Fig. 3a in [11]). This configuration can generate a 6-DoF wrench without over-actuation, simplifying the thrust allocation problem. Furthermore, we also borrowed from Brescianini and D'Andrea the clever mechanical design of the AWG frame (see the upper left part in Fig. 1). Propulsion units are attached to the vertices of an octahedron ($10\,\text{mm}$ diameter carbon fiber tubes on the DextAir robot) in order to be as rotationally invariant as possible. With this configuration, the inertia matrix is simply a multiple of the identity matrix.

Each propulsion unit is made of a pair of coaxial contra-rotating propellers (Graupner 3D 6") in order to cancel unwanted reaction torque and gyroscopic effects. Each propeller is driven by a brushless DC motor (T-Motor F40 Pro II Kv2600) which is connected to an Electronic Speed Controller (ESC, KISS 32A). Since standard ESCs do not regulate the rotational velocity and since the thrust is directly linked to the squared rotational velocity of the propeller, we implemented an outer fast PID speed regulation loop using real-time ESC telemetry data. This regulation is running on an external micro-controller (MCU, Teensy 3.5) at a sampling rate of $500\,\text{Hz}$ acquiring telemetry data through a $115\,200$ bps serial link and sending ESC throttle control input data using the DSHOT600 protocol. The code of the MCU has been developed in our lab for this project and will be open-sourced in a near future.

The AWG is fully autonomous: it carries its own energy source, a $1550\,\text{mA h}$, $11.1\,\text{V}$ lithium polymer battery pack (TATTU 3S1P). It also has an on-board CPU (Raspberry Pi 4B) running high-level control algorithms and communicating with a ground station through Wi-Fi TCP/IP sockets thanks to the open-source Simulink toolbox RPIt [12] developed in our lab. The Raspberry Pi is connected by USB to 2 MCUs regulating the velocity of a total of 12 motors.

The position of the AWG is acquired by an 8-camera Vicon Bonita motion-capture system (see Fig. 2) measuring the 6-DoF pose vector of the AWG with a refresh rate of $200\,\text{Hz}$.

III. Modeling of the AMES

In this section, we derive the model of an Aerial Manipulator with Elastic Suspension (AMES). The spring anchor point is supposed static and the model of the robotic carrier is not considered.

A. Propulsion unit

To model the propulsion unit (see Fig. 2), we are making the following assumptions:

- Due to the coaxial contra-rotating rotor configuration, the reaction torque and gyroscopic effect generated by one rotor are compensated by the other one;

- The total thrust of two contra-rotating propellers behaves like the thrust of a single equivalent propeller;
- The total thrust is proportional to the square of the rotation speed in steady state and during transients.

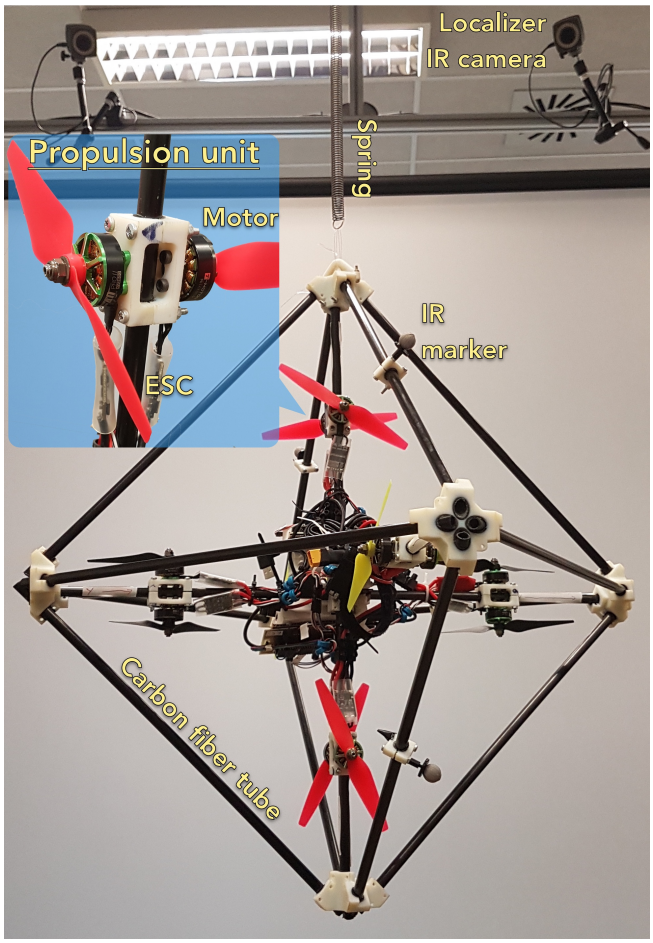

Fig. 2. DextAir prototype.

The measured thrust coefficient a of the two combined contra-rotating propellers is $1.87 \times 10^{-6}\,\mathrm{kg\,m\,rad^{-2}}$. It was identified on a test bench (RCbenchmark 1520 Thrust Stand) modified to carry the dual-motor propulsion unit.

The velocity of the propellers is controlled externally with an anti-windup PID digital loop. A single MCU (PJRC Teensy 3.5) is controlling the velocity of 6 ESCs. So two MCUs are required to control the 12 motors of the AWG. Recent ESC firmware (KISS and BLHeli for example) can send telemetry data on a serial link that contains among other the velocity of the electromagnetic field. Since synchronous motors are used, this velocity is proportional to the rotor mechanical velocity. Our custom code running on the MCU can robustly retrieve this measurement at a frequency of 500 Hz, calculate a throttle value and send it to the ESC using the DSHOT600 digital protocol. The 6 control loops are running synchronously on one MCU thanks to a Direct Memory Access (DMA) mechanism used to generate the DSHOT signal. The ESCs are configured to work in a bidirectional mode (called 3D mode). In this mode the inverter within the ESC works in a 4-quadrant mode. We tuned the PID to obtain a step response shaped like a first order with a 60 ms time constant. Since this response time is many orders of magnitude faster than the mechanical oscillation modes of the AWG, we consider that it is negligible in the remainder of this paper.

B. AWG dynamics

Newton-Euler's equations describing the dynamics of the AWG written in a fixed inertial reference frame R_f are the following (see Fig. 7 for the definition of the frames):

$$\begin{bmatrix} m\mathbb{I}_{3\times3} & \mathbf{0}_{3\times3} \\ \mathbf{0}_{3\times3} & \mathbf{I_f} \end{bmatrix} \begin{bmatrix} \ddot{\mathbf{p}} \\ \dot{\boldsymbol{\omega}} \end{bmatrix} + \begin{bmatrix} \mathbf{0}_{3\times1} \\ \boldsymbol{\omega} \times \mathbf{I_f}\boldsymbol{\omega} \end{bmatrix} + \begin{bmatrix} mg\mathbf{z} \\ \mathbf{0}_{3\times1} \end{bmatrix} - \begin{bmatrix} \mathbf{F_s} \\ \mathbf{N_s} \end{bmatrix} = \begin{bmatrix} \mathbf{F} \\ \mathbf{N} \end{bmatrix} \tag{1}$$

where m is the total mass of the AWG, g the gravitational acceleration, $\mathbf{p}$ the coordinates of the AWG center of gravity G, $\boldsymbol{\omega}$ the angular velocity of the AWG, $\mathbf{I_f}$ the inertia matrix of the AWG expressed in the inertial frame, $\mathbf{z} = [0\ 0\ 1]^T$, $\mathbf{F_s}$ and $\mathbf{N_s}$ the force and the moment applied by the spring on the AWG, $\mathbf{F}$ and $\mathbf{N}$ the force and the torque generated by the propellers on the AWG.

Let $\mathbf{R_{fb}}$ be the rotation matrix from the inertial frame R_f to the body frame R_b, such that ${}^f\mathbf{v} = \mathbf{R_{fb}}\,{}^b\mathbf{v}$. Then, $\mathbf{I_f}$ can be written as:

$$\mathbf{I_f} = \mathbf{R_{fb}} \mathbf{I_b} \mathbf{R_{fb}}^T$$

with $\mathbf{I_b}$ the constant diagonal inertia matrix of the AWG expressed in the body frame R_b.

The force applied by the spring on the AWG can be written as:

$$\mathbf{F_s} = -k\left(\mathbf{OP} - l_0 \frac{\mathbf{OP}}{\|\mathbf{OP}\|}\right)$$

where k is the spring constant, l_0 the unstretched length of the spring, O and P the attachment points of the spring respectively to the carrier and to the body. Thus,

$$\mathbf{OP} = \mathbf{p} + \Delta \mathbf{R_{fb}} \mathbf{z}$$

with Δ the distance between G and P. The moment applied by the spring on the AWG is given by:

$$\mathbf{N_s} = \Delta \mathbf{R_{fb}} \mathbf{z} \times \mathbf{F_{res}}$$

Let $\mathbf{A_b}$ be the matrix that maps the vector $\mathbf{w_2} = [\cdots\ \ w_i|w_i|\ \ \cdots]^T$ of signed squared propeller rotational speeds w_i to the wrench they apply to the AWG:

$$\begin{bmatrix} {}^b\mathbf{F} \\ {}^b\mathbf{N} \end{bmatrix} = \mathbf{A_b} \mathbf{w_2} \tag{2}$$

$$\mathbf{A_b} = a \begin{bmatrix} {}^b\mathbf{u_1} & \cdots & {}^b\mathbf{u_6} \\ {}^b\mathbf{GB_1} \times {}^b\mathbf{u_1} & \cdots & {}^b\mathbf{GB_6} \times {}^b\mathbf{u_6} \end{bmatrix}$$

with a the thrust coefficient, $\mathbf{u_i}$ the axis of the i-th propeller, B_i the center of the i-th propeller.

Thus, using equation (2), equation (1) can be rewritten as:

$$\begin{bmatrix} m\mathbb{I}_{3\times3} & \mathbf{0}_{3\times3} \\ \mathbf{0}_{3\times3} & \mathbf{I_f} \end{bmatrix} \begin{bmatrix} \ddot{\mathbf{p}} \\ \dot{\boldsymbol{\omega}} \end{bmatrix} + \begin{bmatrix} \mathbf{0}_{3\times1} \\ \boldsymbol{\omega} \times \mathbf{I_f}\boldsymbol{\omega} \end{bmatrix} + \begin{bmatrix} mg\mathbf{z} \\ \mathbf{0}_{3\times1} \end{bmatrix} - \begin{bmatrix} \mathbf{F_s} \\ \mathbf{N_s} \end{bmatrix} = \begin{bmatrix} \mathbf{R_{fb}} & \mathbf{0}_{3\times1} \\ \mathbf{0}_{3\times1} & \mathbf{R_{fb}} \end{bmatrix} \mathbf{A}_b\, \mathbf{w_2} \tag{3}$$

Let $\mathbf{x} = [x\ y\ z\ \psi\ \theta\ \phi]^T$ be the vector describing the pose of the AWG, with $\mathbf{p} = [x\ y\ z]^T$ the coordinates of G and $\boldsymbol{\eta} = [\psi\ \theta\ \phi]^T$ a set of Davenport angles. The analytical Jacobian matrix $\mathbf{S}(\boldsymbol{\eta})$ maps the angular velocity vector $\boldsymbol{\omega}$ to the time derivative of the chosen Davenport angles $\dot{\boldsymbol{\eta}}$:

$$\boldsymbol{\omega} = \mathbf{S}(\boldsymbol{\eta})\,\dot{\boldsymbol{\eta}} \tag{4}$$

and so

$$\dot{\boldsymbol{\omega}} = \dot{\mathbf{S}}(\boldsymbol{\eta})\,\dot{\boldsymbol{\eta}} + \mathbf{S}(\boldsymbol{\eta})\,\ddot{\boldsymbol{\eta}} \tag{5}$$

Combining equations (3), (4) and (5), the equations of motion can be expressed using the pose $\mathbf{x}$:

$$\begin{bmatrix} m\mathbb{I}_{3\times3} & \mathbf{0}_{3\times3} \\ \mathbf{0}_{3\times3} & \mathbf{I_f} \end{bmatrix} \begin{bmatrix} \ddot{\mathbf{p}} \\ \dot{\mathbf{S}}\dot{\boldsymbol{\eta}} + \mathbf{S}\ddot{\boldsymbol{\eta}} \end{bmatrix} + \begin{bmatrix} \mathbf{0}_{3\times1} \\ \mathbf{S}\,\dot{\boldsymbol{\eta}} \times \mathbf{I_f}\mathbf{S}\,\dot{\boldsymbol{\eta}} \end{bmatrix} + \begin{bmatrix} mg\mathbf{z} \\ \mathbf{0}_{3\times1} \end{bmatrix} - \begin{bmatrix} \mathbf{F_s} \\ \mathbf{N_s} \end{bmatrix} = \begin{bmatrix} \mathbf{R_{fb}} & \mathbf{0}_{3\times1} \\ \mathbf{0}_{3\times1} & \mathbf{R_{fb}} \end{bmatrix} \mathbf{A}_b\,\mathbf{w_2} \tag{6}$$

After rearranging the terms and left-multiplying equation (6) by $\begin{bmatrix} \mathbb{I}_{3\times3} & \mathbf{0}_{3\times3} \\ \mathbf{0}_{3\times3} & \mathbf{S^T} \end{bmatrix}$ to make the inertia matrix symmetrical, we obtain the dynamic model in its classical formulation:

$$\underbrace{\begin{bmatrix} m\mathbb{I}_{3\times3} & \mathbf{0}_{3\times3} \\ \mathbf{0}_{3\times3} & \mathbf{S}^T\mathbf{I_f}\mathbf{S} \end{bmatrix}}_{\mathbf{M}(\mathbf{x})} \begin{bmatrix} \ddot{\mathbf{p}} \\ \ddot{\boldsymbol{\eta}} \end{bmatrix} + \underbrace{\begin{bmatrix} \mathbf{0}_{3\times1} \\ \mathbf{S}^T(\mathbf{I_f}\dot{\mathbf{S}}\dot{\boldsymbol{\eta}} + \mathbf{S}\,\dot{\boldsymbol{\eta}} \times \mathbf{I_f}\mathbf{S}\,\dot{\boldsymbol{\eta}}) \end{bmatrix}}_{\mathbf{C}(\mathbf{x},\dot{\mathbf{x}})\dot{\mathbf{x}}} + \underbrace{\begin{bmatrix} mg\mathbf{z} - \mathbf{F_s} \\ -\mathbf{N_s} \end{bmatrix}}_{\mathbf{G}(\mathbf{x})} = \underbrace{\begin{bmatrix} \mathbb{I}_{3\times3} & \mathbf{0} \\ \mathbf{0} & \mathbf{S}^T \end{bmatrix} \begin{bmatrix} \mathbf{R_{fb}} & \mathbf{0}_{3\times1} \\ \mathbf{0}_{3\times1} & \mathbf{R_{fb}} \end{bmatrix} \mathbf{A}_b\,\mathbf{w_2}}_{\tilde{\mathbf{A}}(\mathbf{x})} \tag{7}$$

IV. Control law

This section presents the control strategy used to follow a reference trajectory and to reject disturbances. A computed torque (feedback linearization) control law is used. The dynamic model (7) in its classical form is the following:

$$\mathbf{M}(\mathbf{x})\ddot{\mathbf{x}} + \mathbf{C}(\mathbf{x},\dot{\mathbf{x}})\dot{\mathbf{x}} + \mathbf{G}(\mathbf{x}) = \boldsymbol{\tau} \tag{8}$$

with $\boldsymbol{\tau} = \tilde{\mathbf{A}}(\mathbf{x})\mathbf{w_2}$.

To follow a desired trajectory $\mathbf{x}_d$, the following computed torque control law is applied:

$$\boldsymbol{\tau} = \hat{\mathbf{M}}(\ddot{\mathbf{x}}_d + \mathbf{u}) + \hat{\mathbf{C}}\dot{\mathbf{x}} + \hat{\mathbf{G}} \tag{9}$$

with $\mathbf{u}$ a feedback control input, $\hat{\mathbf{M}}$, $\hat{\mathbf{C}}$ and $\hat{\mathbf{G}}$ are the estimates of $\mathbf{M}$, $\mathbf{C}$ and $\mathbf{G}$ in (8).

The signal $\mathbf{u}$ is the result of a Proportional-Derivative (PD) control law: $\mathbf{u} = \mathbf{k}_d\dot{\mathbf{e}} + \mathbf{k}_p\mathbf{e}$, with $\mathbf{e} = \mathbf{x}_d - \mathbf{x}$ the pose error signal, $\mathbf{k}_p$ and $\mathbf{k}_d$ tunable proportional and derivative gains. Thus the control law becomes (see Fig. 3):

$$\boldsymbol{\tau} = \hat{\mathbf{M}}(\ddot{\mathbf{x}}_d + \mathbf{k}_d\dot{\mathbf{e}} + \mathbf{k}_p\mathbf{e}) + \hat{\mathbf{C}}\dot{\mathbf{x}} + \hat{\mathbf{G}} \tag{10}$$

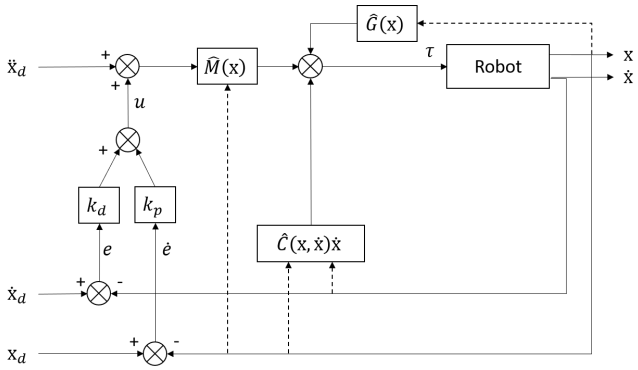

Fig. 3. Computed torque control law block diagram.

A. Stability analysis

1) With perfect model: Assuming a perfect knowledge of the system model, the proof of stability is straightforward. By substituting equation (10) in equation (8), we obtain the closed-loop error dynamics:

$$\ddot{\mathbf{e}} + \mathbf{k}_d\dot{\mathbf{e}} + \mathbf{k}_p\mathbf{e} = 0$$

The error tends towards zero if $\mathbf{k}_d$ and $\mathbf{k}_p$ are both positive definite (for the proof, consider the Lyapunov function $V = \frac{1}{2}\dot{\mathbf{e}}^T\dot{\mathbf{e}} + \frac{1}{2}\mathbf{e}^T\mathbf{k}_p\mathbf{e}$): the system is asymptotically stable for $\mathbf{k}_d > 0$ and $\mathbf{k}_p > 0$.

2) Sensitivity to spring stiffness: Parameter values may be different between the real plant and the model due to identification errors. Simulations show that the spring stiffness is a very sensitive parameter: a small overestimation may yield instability. Let's restrict, without loss of generality, the movement to the vertical axis. The system is modeled as a harmonic oscillator with an external force. Let's assume $z_d = 0$. In this particular case, the equation of motion is given by:

$$m\ddot{z} + kz = F$$

The computed torque is calculated as following:

$$F = m(-k_d\dot{z} - k_pz) + k'z$$

Substitution yields:

$$\ddot{z} + k_d\dot{z} + \left(k_p + \frac{k - k'}{m}\right)z = 0$$

This equation shows that the closed loop is stable if $k_p > \frac{k'-k}{m}$. So, to increase the robustness of the system, it is better to slightly underestimate the stiffness of the spring.

V. Simulator and Model Validation

A dynamic simulator is implemented with MATLAB/Simulink in order to i) validate the open-loop model (6) by comparing simulated and experimental responses; ii) validate the control law (10), since motor dynamics are not taken into account in the proof of stability. Some assumptions are made:

- The 12 rotor velocity loops are modeled as a first order system with a $60\,\mathrm{ms}$ time constant;

- The 12 control signals sent to 2 MCU boards (a rotational velocity reference) can vary between 1250 rpm and 25 000 rpm.

In order to check the validity of the system equations and assess the simulator accuracy, open-loop simulated and experimental responses are compared in Fig. 4. The good fit between the curves validates that dynamic parameters given in table I are estimated with a good accuracy.

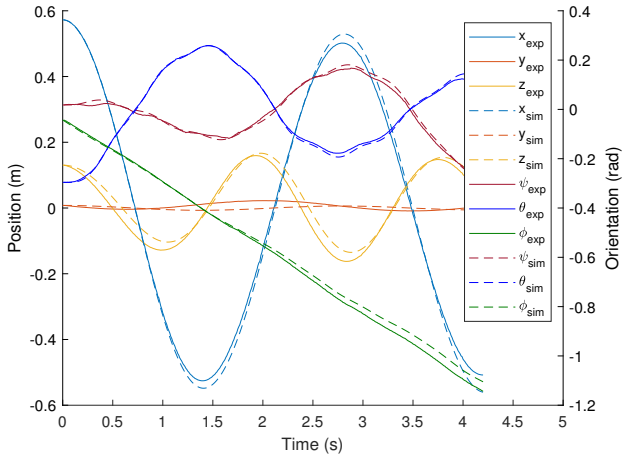

Fig. 4. Comparison between simulated and experimental open-loop response.

TABLE I
MODEL PARAMETERS

Parameter	Description	Value
m	Total mass	$2.07\,\mathrm{kg}$
I_x,I_y,I_z	Moments of inertia	$5.04 \times 10^{-2}\,\mathrm{kg\,m^2}$
k	Spring stiffness	$22.5\,\mathrm{kg\,m^{-1}}$
L	Propeller axis to CoG distance	$0.16\,\mathrm{m}$
Δ	Spring to CoG distance	$0.32\,\mathrm{m}$
a	Thrust coefficient	$1.9\,\mu\mathrm{N\,rad^{-2}\,s^2}$

To test the control law, a path tracking simulation is done using a square reference. To avoid saturation, velocity is set to zero at the corners. The robot takes $1.5\,\mathrm{s}$ for each edge, then waits $3\,\mathrm{s}$ at each corner. To compensate for tracking errors caused by motor dynamics (these dynamics are neglected in this preliminary study), an integrator is added to the controller. The tuning values of the controller are displayed in table II. The trajectory and the tracking errors are respectively shown in Fig. 5 and 6. Note that the chosen angles are consecutive rotations respectively around the initial $\vec{x}$ (ψ), $\vec{y}$ (θ) and $\vec{z}$ (ϕ) axes.

VI. PRELIMINARY EXPERIMENTAL RESULTS - STABILIZATION

Only stabilization experiments are presented in this section. These experiments are displayed in the video associated to this paper. Since the reference is equal to zero, the feedforward action of the computed torque control law disappears. Experimental PD controller tuning parameters are displayed

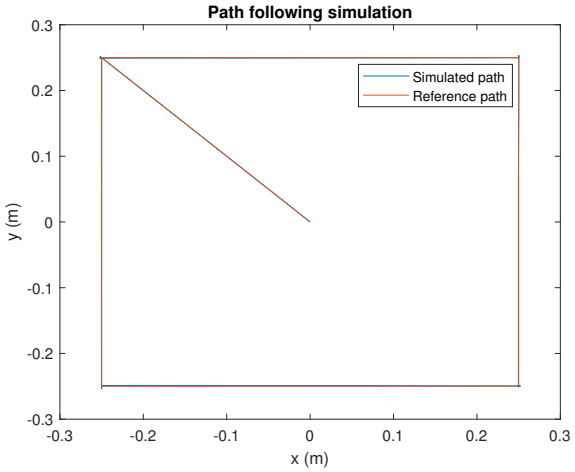

Fig. 5. Path following simulation.

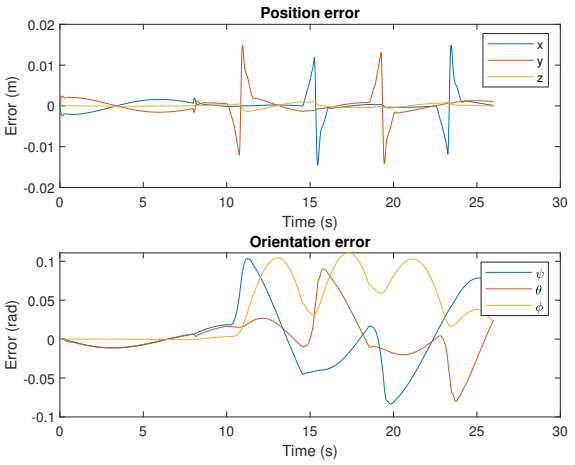

Fig. 6. Path following errors in simulation.

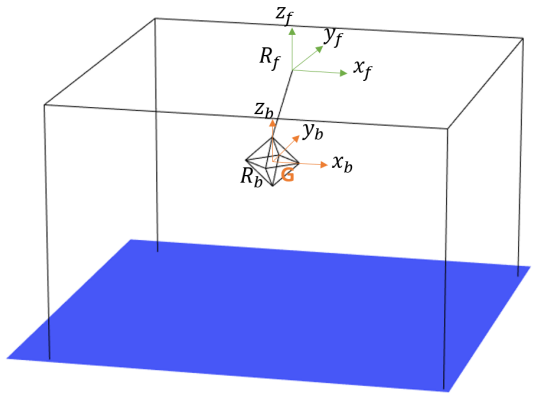

Fig. 7. 3D visualizer view.

TABLE II

PID VALUES FOR PATH FOLLOWING

Control variable	P	I	D
x	2	6	18
y	2	6	18
z	2	6	12
ψ	2	5	12
θ	2	5	12
ϕ	2	5	33.6

in table III. To avoid the chattering due to noise in the motion-tracking system measurement, a dead zone is added to the pose error (but does not impact the derivative of the error): $2\,\mathrm{cm}$ for position errors and $2°$ for orientation errors.

TABLE III

PD VALUES FOR STABILIZATION

Control variable	P	D
x	0.1	3
y	0.1	3
z	0.1	3
ψ	0	0.07
θ	0	0.07
ϕ	0.1	0.07

Fig. 8 and 9 show the damping of the oscillations in closed loop with respect to the free response. Moreover, we can notice that the yaw angle ψ (around the vertical axis) is not diverging anymore. Fig. 10 compares simulation and experimental results for a translational disturbance rejection in closed loop. This validates the good fit between experiment and simulation despite a steady-state error in the experimental results due to the dead zone.

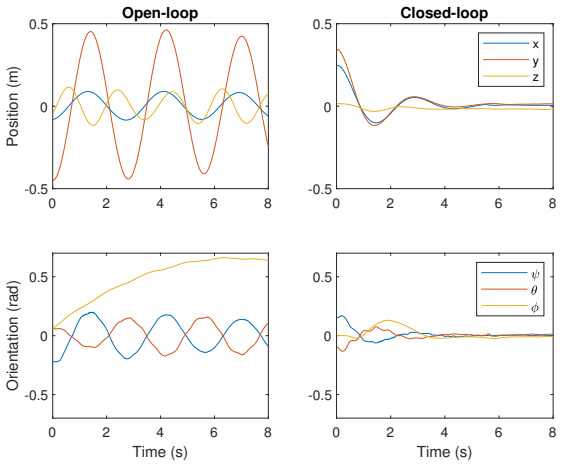

Fig. 8. Comparison between open-loop and closed-loop response with a position perturbation.

VII. CONCLUSION - FUTURE WORK

This preliminary study shows that propellers driven by brushless DC motors, like those used for drones, allows for generating a wrench on a dynamic range large enough to efficiently regulate the 6-DoF pose of an Aerial Manipulator

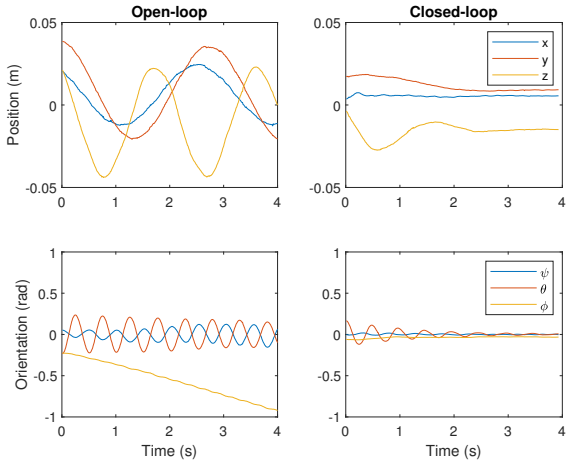

Fig. 9. Comparison between open-loop and closed-loop response with an orientation perturbation.

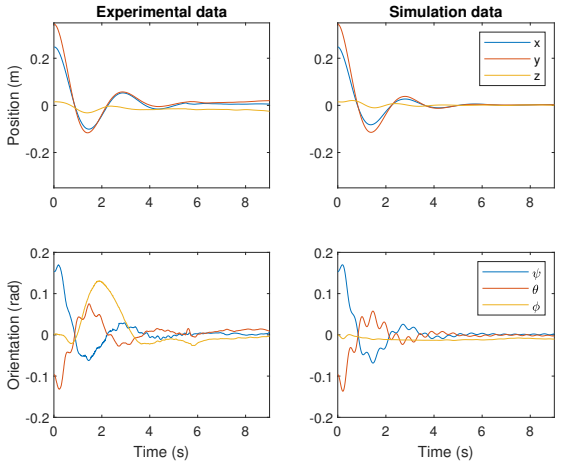

Fig. 10. Closed-loop comparison between simulation and experience with a position perturbation.

suspended by a spring. However, some points still need to be investigated. The control law may be improved by taking into account the dynamics of the velocity-controlled rotors. Trajectory tracking needs to be assessed experimentally. Furthermore, the robotic carrier needs still to be implemented and a control law combining the fast motion of the AWG and the slow motion of the robotic carrier needs to be studied.

ACKNOWLEDGMENT

This work is part of the e-VISER project (ANR-17-CE33-0008) funded by the French National Research Agency.

REFERENCES

[1] F. Ruggiero, V. Lippiello, and A. Ollero, "Aerial manipulation: A literature review," *IEEE Robotics and Automation Letters*, 2018.

[2] M. Orsag, C. Korpela, P. Oh, and S. Bogdan, *Aerial Manipulation*, M. Grimble and M. Johnson, Eds. Springer International Publishing AG, 2017. [Online]. Available: http://link.springer.com/10.1007/978-3-319-61022-1

[3] M. J. Kim, J. Lin, K. Kondak, D. Lee, and C. Ott, "Oscillation Damping Control of Pendulum-like Manipulation Platform using Moving Masses," *IFAC-PapersOnLine*, vol. 51, no. 22, pp. 465–470, 2018.

[4] K. Zhang, P. Chermprayong, T. M. Alhinai, R. Siddall, and M. Kovac, "SpiderMAV: Perching and stabilizing micro aerial vehicles with bio-inspired tensile anchoring systems," in *2017 IEEE/RSJ International Conference on Intelligent Robots and Systems (IROS)*. IEEE, sep 2017, pp. 6849–6854. [Online]. Available: http://ieeexplore.ieee.org/document/8206606/

[5] Y. Sarkisov, M. J. Kim, D. Bicego, D. Tsetserukou, C. Ott, A. Franchi, and K. Kondak, "Development of SAM: cable-Suspended Aerial Manipulator," in *2019 International Conference on Robotics and Automation (ICRA)*, 2019, pp. 5323–5329. [Online]. Available: https://www.icra2019.org

[6] R. Miyazaki, R. Jiang, H. Paul, Y. Huang, and K. Shimonomura, "Long-reach aerial manipulation employing wire-suspended hand with swing-suppression device," *IEEE Robotics and Automation Letters*, vol. 4, no. 3, pp. 3045–3052, 2019.

[7] G. El-Ghazaly, M. Gouttefarde, and V. Creuze, "Hybrid cable-thruster actuated underwater vehicle-manipulator systems: A study on force capabilities," in *2015 IEEE/RSJ International Conference on Intelligent Robots and Systems (IROS)*, IEEE. IEEE, 2015, pp. 1672–1678. [Online]. Available: http://ieeexplore.ieee.org/document/7353592/

[8] H. Sellet, I. Khayour, L. Cuvillon, S. Durand, and J. Gangloff, "Active damping of parallel robots driven by flexible cables using cold-gas thrusters," in *2019 International Conference on Robotics and Automation (ICRA)*, May 2019, pp. 530–536.

[9] J. Begey, L. Cuvillon, M. Lesellier, M. Gouttefarde, and J. Gangloff, "Dynamic control of parallel robots driven by flexible cables and actuated by position-controlled winches," *IEEE Transactions on Robotics*, vol. 35, no. 1, pp. 286–293, Feb 2019.

[10] G. El-Ghazaly, M. Gouttefarde, V. Creuze, and F. Pierrot, "Maximum wrench feasible payload in cable-driven parallel robots equipped with a serial robot," in *2016 IEEE International Conference on Advanced Intelligent Mechatronics (AIM)*, July 2016, pp. 1572–1578.

[11] D. Brescianini and R. D'Andrea, "An omni-directional multirotor vehicle," *Mechatronics*, vol. 55, pp. 76–93, 2018.

[12] J. Gangloff, A. Yigit, and M. Lesellier, "RPIt," Strasbourg, France, 2019. [Online]. Available: https://github.com/jacqu/RPIt/